First Direct Observational Evidence for Secondary Gravity Waves Generated by Mountain Waves over the Andes

Masaru Kogure[1], Jia Yue[2,3], Takuji Nakamura[4,5], Lars Hoffmann[6], Sharon L. Vadas[7], Yoshihiro Tomikawa[4,5], Mitsumu K. Ejiri[4,5], Diego Janches[2]

[1]Department of Earth and Planetary Science, Kyushu University, 744 Motooka Nishi-ku, Fukuoka, Japan

[2]NASA Goddard Space Flight Center, 8800 Greenbelt Rd, Greenbelt, MD, USA

[3]Catholic University of America, 620 Michigan Ave NE, Washington, DC, USA

[4]National Institute of Polar Research, 10-3, Midori-cho, Tachikawa-shi, Tokyo, Japan

[5]The Graduate University for Advanced Studies, SOKENDAI, 10-3, Midori-cho, Tachikawa-shi, Tokyo, Japan

[6]Forschungszentrum Jülich, Wilhelm-Johnen-Straße, 52428 Jülich, Germany

[7]NorthWest Research Associates, 3380 Mitchell Lane, Boulder, CO, USA

Corresponding author: Masaru Kogure (kogure.masaru.695@m.kyushu-u.ac.jp)

Key Points:

- VIIRS captured nightglow concentric ring-like gravity waves in mesopause east of Southern Andes during intense winter mountain wave event.
- Mountain waves observed by AIRS likely broke while the waves were propagating upward and eastward.
- Concentric ring-like gravity waves captured by VIIRS were likely generated by local body forces created by mountain wave breaking.

Abstract

A mountain wave with a significant brightness temperature amplitude and ~500 km horizontal wavelength was observed over the Andes on 24–25 July 2017 in AIRS/Aqua satellite data. In the MERRA-2 reanalysis data, the intense eastward wind flowed over the Andes. VIIRS/Suomi-NPP did not detect the mountain waves; however, it observed concentric ring-like waves in the nightglow emissions at ~87 km with ~100 km wavelengths on the same night over and leeward of the Southern Andes. A ray tracing analysis showed that the mountain waves propagated to the east of the Andes, where concentric ring-like waves appeared above a region of mountain wave breaking. Therefore, the concentric ring-like waves were likely secondary waves generated by momentum deposition that accompanied mountain wave breaking. These results provide the first direct evidence for secondary gravity waves generated by momentum deposition.

Plain Language Summary

A recent model study (Vadas and Becker, 2019) showed that mountain waves created over the Andes broke in the stratosphere and mesosphere, thereby depositing their momentum and creating "secondary" gravity waves. These waves then propagated into the lower thermosphere and created tertiary (or higher-order) waves, some of which propagated to the upper thermosphere. This vertical multistep coupling mechanism is likely important for creating ionospheric disturbances in the F region. However, observational evidence supporting this mechanism is lacking. The purpose of this study is to show observational evidence using data from two satellite instruments: AIRS/Aqua and VIIRS/Suomi-NPP. AIRS captured a mountain wave with a significant amplitude in the stratosphere over the Andes on 24-25 July 2017. VIIRS/Suomi-NPP did not detect the mountain waves but instead observed concentric ring-like gravity waves in the mesosphere on the leeward of the Andes. The concentric ring-like structure is one of the features of secondary waves created from momentum deposition that accompanies breaking gravity waves; thus, we conclude that the observed gravity waves were likely secondary gravity waves. These observational results provide the first direct evidence for secondary gravity waves generated by momentum deposition from breaking mountain waves and support the vertical multistep coupling mechanism.

Keywords: Middle atmosphere, Secondary gravity wave, AIRS/Aqua, VIIR/Suomi-NPP, Andes, Mountain wave

1 Introduction

Gravity waves (GWs) drive atmospheric circulation, which affects the temperature structure and distribution of chemical components (*Fritts and Alexander*, 2003; *Butchart et al.*, 2010). Mountain waves (MWs) are one type of GW and are emitted from wind flowing over a topography. MWs transport a significant amount of momentum from the lower to the middle atmosphere, a process that is typically parameterized in numerical models (*Fritts and Alexander*, 2003; *Alexander et al.*, 2010; *Butchart et al.*, 2010). MWs have been studied using various observations, theoretical considerations, and numerical simulations over the last few decades. Satellite observational instruments such as the atmospheric infrared sounder (AIRS) (*Hoffmann et al.*, 2013; *Ern et al.*, 2017), microwave limb sounder (MLS) (*Wu and Eckermann,* 2008), and sounding of the atmosphere using broadband emission radiometry (SABER) (*Preusse et al.,* 2009)) have provided global maps of GW activity. They have shown that the Andes are one of the most intense GW activity regions in the middle atmosphere due to MWs caused by wind

flowing over the Andes. The high GW energy region extends leeward of the Andes due to the polar night jet (*Sato et al.*, 2012).

MWs theoretically have quasi-stationary ground-based phase velocities and may encounter critical levels in weak wind layers (*Fritts and Alexander*, 2003). When GWs break, they not only accelerate background circulation but also excite secondary GWs (*Vadas et al.*, 2003; *Bacmeister and Schoeberl*, 1989; *Heale et al.*, 2020a). A few observational studies have shown statistically that secondary GWs are likely associated with MW events over the Andes. *de Wit et al.* (2017) estimated GW momentum flux over the Southern Andes using meteor radar wind measurements and found a significant vertical flux of eastward momentum in the mesosphere and lower thermosphere. Tropospheric GW sources cannot explain this eastward momentum flux because a polar vortex is present over the Southern Andes. *de Wit et al.* (2017) argued that secondary GWs contributed to this eastward momentum flux. *Liu et al.* (2019) found high MW activity in the Austral winter over the Andes up to 55 km altitude that attenuated between 55-65 km altitude. GW activity increased again above 65 km of altitude with a westward tilt. Their results suggest that breaking MWs over the Andes generate secondary GWs. However, to the best of our knowledge, no direct nadir simultaneous observations of a MW and the corresponding secondary wave have been reported.

Two mechanisms can generate secondary GWs: nonlinear fluid interactions and local body forces (*Vadas and Becker.*, 2018; *Heale et al.*, 2020a). Nonlinear interactions result in a cascade of energy to smaller-scales and the generation of secondary GWs that have smaller scales than those of the primary GWs (*Fritts et al.*, 1994; *Andreassen et al.*, 1998; *Fritts et al.*, 1998). *Bossert et al.* (2015) observed small-scale GWs in a warm phase front of a MW over Mount Cook by using Advanced Mesosphere Temperature Mapper observations aboard an aircraft. *Heale et al.* (2017) simulated this event by using a 2-D nonlinear model and found that secondary GWs were created in the warm phase where instabilities occurred due to primary GWs breaking. The secondary GWs had smaller horizontal wavelengths than the wavelength of the MW by one order of magnitude and had broad phase velocity spectra.

Alternatively, secondary GWs can also be created by local body forces such as temporally and spatially localized wave drag, created by the deposition of momentum that accompanies primary GW breaking. A local body force creates an imbalance in the flow so that the resultant wave-mean flow interaction generates secondary GWs (*Vadas et al.*, 2003, 2018). The latter secondary GW spectra have broad horizontal phase speeds, periods, and wavelengths, and propagate in all azimuths except perpendicular to the body force direction. These spectra depend on the size and duration of the local body force. Some secondary GWs can avoid breaking over large distances and can "carry" momentum and energy into the upper atmosphere. *Vadas et al.* (2003, 2018) simulated secondary GWs created by a local body force using a Fourier-Laplace model. They found that the peaks of the horizontal and vertical wavelength spectra were ~2 times larger than the horizontal and 1-2 times larger than the vertical sizes of the local body force. The peak of the period spectrum was the characteristic period of the body force unless the duration was longer. Note that the size of a body force can be smaller than the primary GW horizontal wavelength if constructive/destructive interference occurs between several primary wave packets (*Vadas and Crowley*, 2010).

Vadas and Becker (2019) showed that MWs generated over the Southern Andes break near the stratopause, thereby generating secondary GWs from local body forces. These secondary GWs then propagated higher, where they broke and dissipated at an altitude between

~80-130 km, thereby creating tertiary GWs that propagated higher into the thermosphere. Such higher-order GWs were likely observed by the GOCE satellite (*Vadas et al., 2019*) as "hotspot" traveling atmospheric disturbances, (*Trinh et al.*, 2018), which was verified by a recent modeling study (*Becker and Vadas*, JGR, submitted). Thus, this strongly suggests that momentum and energy are transported into the upper thermosphere via a vertical multistep coupling mechanism (see Figure 21 in *Vadas and Becker*, 2019).

Using a high-resolution model, *Vadas et al.* (2018) demonstrated that secondary GWs have "fishbone structures" in vertical time slices, which indicates that secondary GWs radiate up and down from primary GW breaking regions. They also found several fishbone structures near the winter stratopause over McMurdo in lidar data. Secondary GWs from MW breaking over the Andes were simulated using a GW-resolving general circulation model (*Becker and Vadas,* 2018). *Vadas and Becker* (2019) showed that secondary GWs had partial concentric ring-like structures. A partial concentric ring-like GW was captured over Chile in OH imager data, and no convection appeared near the OH imager site (*Vargas et al.*, 2016). They inferred that the ring-like GW was generated by a primary GW breaking (possibly generated by convection over Bolivia), although they did not capture the primary GW.

The purpose of this study is to provide the first direct observational evidence that ring-like secondary GWs in the mesopause are created from MWs over the Andes, similar to *Vadas and Becker* (2019). According to their model results, the strong eastward wind flowing over the Andes creates MWs with large amplitudes, and the MWs propagate upward and break at 50-80 km altitude. The momentum deposition that accompanies this breaking process generates local body forces that excite secondary GWs with partial concentric ring-like structures. Some of these secondary GWs then propagate to 100 km. Observations from two satellite instruments, AIRS and the Visible/Infrared Imaging Radiometer Suite (VIIRS), were used to capture both MWs and secondary GWs. AIRS can observe GWs at an altitude range of approximately 20-50 km, and observed MWs during this event. VIIRS observes OH airglow intensity and captured secondary GWs with ring-like structures at an altitude of ~87 km during this event.

2 Satellite observations of GWs: AIRS and VIIRS

2.1 Atmospheric Infrared Sounder (AIRS)

The AIRS instrument aboard the NASA Aqua satellite (*Aumann et al., 2003*; *Chahine et al.,* 2006) measures infrared radiance spectra in three spectral bands between 3.74 and 15.4 μm. Aqua has an orbit period of ~100 min, with local equatorial crossing times of ~1:30 PM and 1:30 AM. AIRS uses cross-track scanning, with each scan consisting of 90 footprints over 1,780 km of ground distance and a separation of 18 km of along-track distance. The footprint size varies between 14×14 km^2 at nadir and 21×42 km^2 at the edges of the scan. AIRS measurements in the 4.3 and 15 μm CO_2 bands have been applied in various studies of stratospheric GWs. Here, $15\mu m$ brightness temperature data averaged over two sets of AIRS channels were used to investigate MWs. First, the brightness temperatures observed in multiple AIRS channels were averaged to reduce the measurement noise. Two channel sets were used for averaging, with temperature kernel functions peaking in two layers around ~23 and ~40 km of altitude. The weighing functions have typical full widths at half maximum of ~15 km and therefore represent mean temperatures over the altitude ranges of 17-32 and 34-49 km, respectively. Second, a fourth-order polynomial fit was subtracted for each across-track scan to remove the background temperatures. The remaining brightness temperature perturbations provide a measure of GWs

with vertical wavelengths longer than 10-15 km and horizontal wavelengths longer than 30-80 km. The AIRS/Aqua observations of GWs are described in more detail by *Hoffmann et al.* (2013, 2017).

2.2 Visible/Infrared Imaging Radiometer Suite (VIIRS)

The VIIRS instrument aboard the NOAA/NASA Suomi-NPP satellite, provides global coverage of visible and infrared wavelength spectra (*Miller et al*., 2015). Its orbit period and local equatorial crossing times are almost the same as Aqua's. VIIRS has 22 channels ranging between 0.41 and 12.01 μm. The day/night band (DNB) sensor is one of the channels and can detect very faint light within 0.505-0.89 μm; therefore, the DNB sensor can capture OH airglow intensity modulated by GWs at an altitude of ~87 km. The horizontal spatial resolution and coverage of the DNB sensor is high ($0.74 \times 0.74 km^2$ and a 3,000 km across-track swath width) and is preserved across the entire swath. Thus, the DNB sensor can capture very small GWs with a horizontal wavelength of several kilometers. In terms of the minimum vertical wavelength (λ_z) of GWs, the ability of the DNB to detect OH airglow intensity modulation depends on the OH airglow thickness so the DNB can typically detect GWs with $\lambda_z \geq 10$ km.

However, DNB also captures reflections from clouds. Tropospheric clouds frequently have wave structures, which makes it difficult to distinguish them from GW modulations in the OH airglow layer. The M15 band sensor is one of the 22 channels in VIIRS and can detect cloud infrared brightness signals (9.8–11.8 μm). This sensor enables us to distinguish GW modulation in the OH airglow layer from cloud reflections.

3 AIRS and VIIRS observations of primary and secondary GWs

3.1. GWs with strong amplitudes captured by AIRS on 24-25 July 2017

AIRS captured MWs with strong amplitudes over the Southern Andes on 24 July 2017, 18:32–18:42 UT and 25 July 2017, 05:43–05:53 UT. Figures 1 (a) and (b) show brightness temperature perturbations at ~23 and ~40 km altitudes on 24 July, respectively. Figures 1 (c) and (d) show the perturbations at the same altitudes on 25 July. The GWs were present directly above the Andes in both layers at both observation times, although the GWs on 25 July were further southward. The GW wavefronts were almost parallel to the Andes mountain chain, which extends from 10°N to 55°S on the west side of the South American continent. Figures 1 (e) and (f) show the horizontal wind in MERRA-2 at 2 km altitude at 12 UT on 24 July and at 0 UT on 25 July, respectively. The eastward tropospheric winds over the Andes are strong (~20–40 m s^{-1}). Such wind conditions are favorable for the occurrence of a strong MW event (*Vadas and Becker*, 2019). A backward GW ray tracing simulation was performed with the same model, initial GWs parameters, and background meteorological conditions in Section 4. The ray tracing result showed that the observed GWs originated from the Andes, which suggests that the GWs were MWs. The strong wind region over the Andes moved southward between 12 UT on 24 July and 0 UT on 25 July, and the observed GWs also moved southward on 25 July in conjunction with the strong wind (Figure 1 (f)). Thus, the observed GWs lasted at least ~11 h and were most likely MWs.

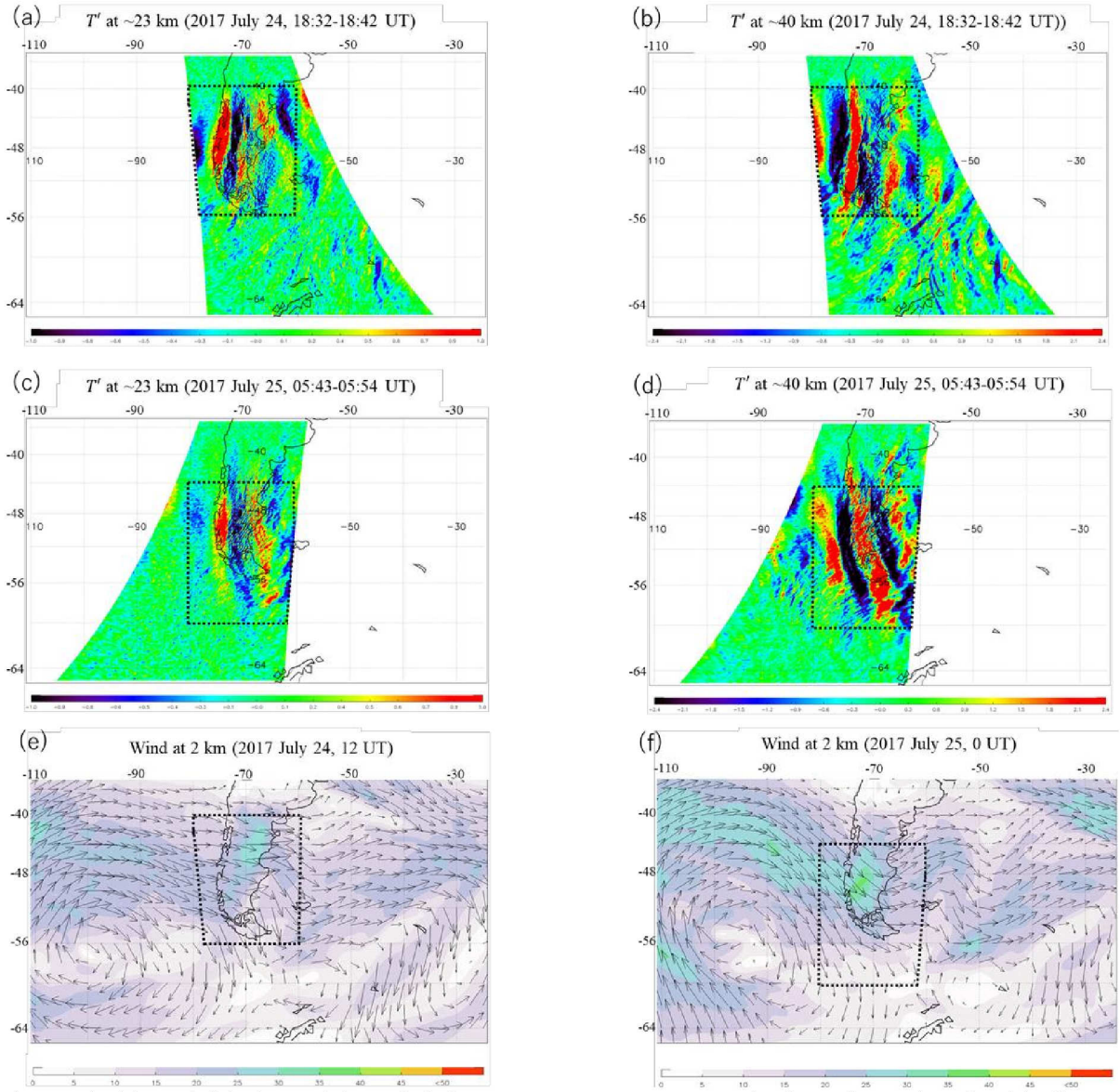

Figure 1. (a) and (b) show 15 μm brightness temperature perturbations from AIRS with GWs at altitudes of ~23 and ~40 km at 18:32-18:42 UT on 24 July 2017, respectively. (c) and (d) show the same as a and b, but at 05:43-05:54 on 25 July 2017. (e) and (f) show the MERRA-2 winds at 2 km altitude at 12 UT on 24 July and 0 UT on 25 July, respectively.

3.2. Concentric ring-like waves captured by VIIRS

Suomi-NPP passed over the Andes between 04:15-04:26 UT on 25 July 2017. Before this time, MWs were present for many hours (Figure 1). Figure 2 (a) shows the OH airglow perturbations where waves are present at 30— 70°W, 48— 64°S. Their wavelengths are approximately 100 km so a bandpass Butterworth filter, with a bandpass between 50 and 220 km, was applied to the OH intensity perturbations to retrieve the wave structures (Figure 2 (b)). Many waves overlap the leeward side of the Andes. The red dashed lines in Figure 2 (b) indicate some of these waves. Most are curved structures. Figure 2 (c) shows the brightness temperatures

from the M15 channel at the same time as Figure 2 (a) and (b). Some wave-like cloud structures can be seen in Figure 2 (c). The red dashed lines in Figure 2 (c) indicate examples of wave-like cloud structures. The same structures are present in the OH intensity in Figure 2 (a) and (b) and are therefore not created by GWs, but rather by reflections of clouds. However, the fine wave structures extending leeward are not found in Figure 2 (c) and are therefore structures created by GWs.

One of the main GW sources near the winter tropopause is geostrophic adjustment of the tropospheric jet. *O'Sullivan and Dunkerton* (1995) found that GWs are emitted from the jet exit region, and have curved fronts. However, their wavefronts are typically perpendicular to the polar night jet that is in the zonal direction. Other potential sources for the observed GWs are secondary generation from temporally and spatially localized momentum deposition (*Vadas et al.*, 2003, 2019) and deep convection (*Taylor and Hapgood*, 1988). One of the main features of both mechanisms is a curved wavefront, i.e., a partial concentric ring, which appears in Figure 2(b). This allows the apparent centers of the concentric ring structure to be determined. A concentric ring structure is distorted and moves leeward from the actual epicenter of a wave and has been shown to occur when concentric GWs propagate in a strong wind (*Vadas et al.*, 2009; *Heale et al.*, 2020b), and likely occurs here from the polar night jet. In the case of those studies, concentric GWs were created by deep convection. However, deep convection is unlikely to occur at $\sim 50°S$ during July, which is wintertime in the southern hemisphere, and there was no deep convection in Figure 2 (c). In addition, a transmission diagram was calculated from MERRA-2 data in accordance with *Tomikwa* (2015) and shows that GWs with 80–120 km wavelengths and east-to-south phase velocities hardly penetrated the stratosphere from the tropopause around the Southern Andes (not shown). Thus, the concentric ring-like GWs observed here are likely not convective GWs. These ring-like GWs are probably secondary GWs generated by local body forces created from MWs breaking.

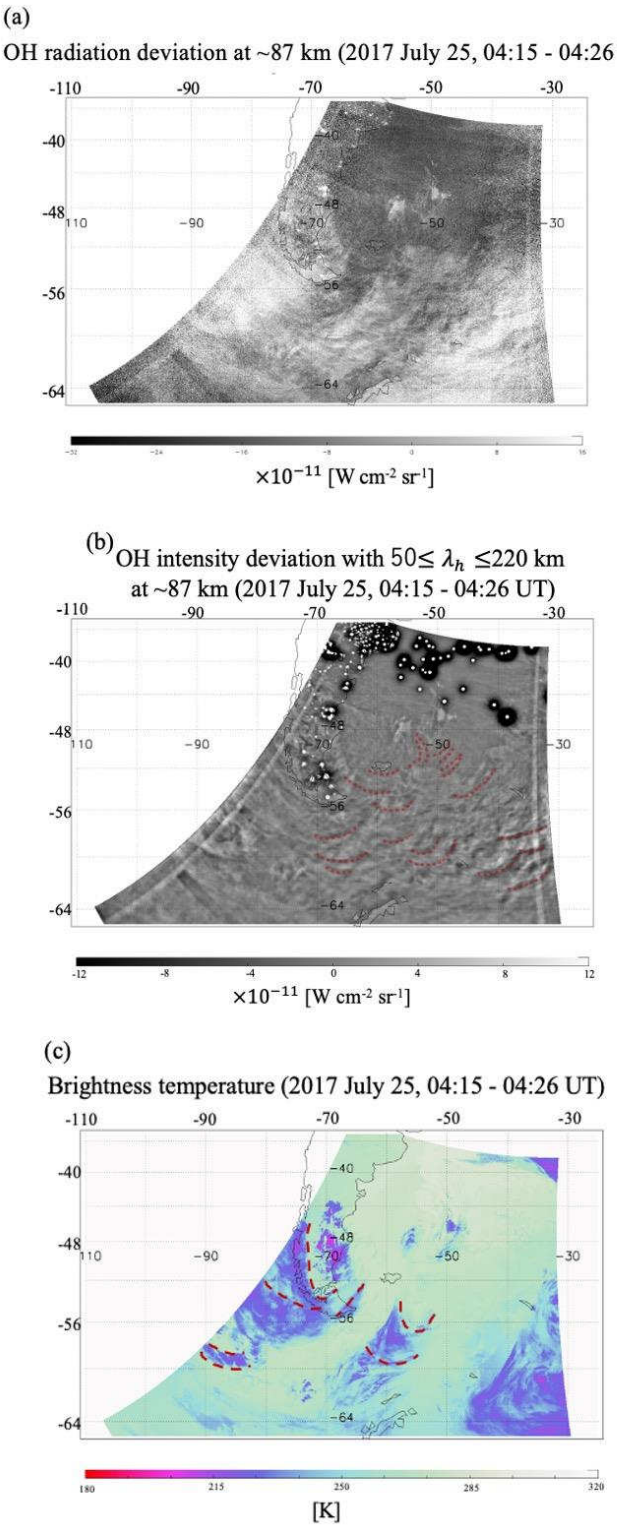

Figure 2. (a) OH intensity deviation at ~87 km altitude at 04:15-04:26 on 25 July 2017. (b) The same as in (a), but the deviations have been filtered with a bandpass Butterworth filter, with a bandpass between 50 and 220 km. (c) Brightness temperatures of clouds at the same time at 9.8-11.8 μm.

4 MWs Breaking

The AIRS observations show MWs, and the VIIRS observations show concentric ring-like waves with multiple apparent centers leeward of the Andes. These features suggest that MWs propagate and break in the stratosphere or lower mesosphere, where they create local body forces. *Sato et al.* (2012) pointed out that MWs over the Andes preferentially propagate leeward due to refraction caused by wind shear of the polar night jet. Using a GW-resolving global circulation model, *Vadas and Becker* (2019) demonstrated that local body forces caused by MWs breaking over the Andes extended leeward at an altitude range of 50-80 km (Figures 8 and 9 in *Vadas and Becker* (2019)). That study also showed that these forces were located at the center of concentric ring-like GWs, which suggests that the ring-like GWs are secondary GWs. Each body force excites secondary GWs with concentric ring-like structures, as shown in *Vadas et al.* (2018). The MWs over the Andes tend to break above the altitude where the polar night jet is at a maximum during winter due to convective instability or critical level filtering (*Vadas and Becker*, 2019). However, weak-amplitude MWs can also propagate into the OH layer if no wind reversals occur (*Smith et al.*, 2009; *Bossert et al.*, 2015). Here, the VIIRS observations showed that stationary MWs were not present near the mesopause.

To estimate the paths of the MWs and their breaking/saturation locations or local body force locations, a forward GW ray tracing simulation was performed. Our ray tracing model is the same as that of *Kogure et al.* (2018), and its mathematical theory is based on *Marks and Eckerman* (1995) and *Dunkerton* (1984). The background wind and temperature were obtained from the MERRA-2 reanalysis. The MERRA-2 data in altitudes of ~68-75 km are uncertain due to the upper boundary condition (*Gelaro et al.*, 2017). The background fields were defined as mean values from 18 UT on 24 July to 06 UT on 25 July, the period during which the MWs were observed. The ground-based initial period of the MWs was assumed to be 0 s because the MWs are approximately stationary (*Dunkerton*, 1984), and the sign of their vertical group velocity is upward. The initial altitude for the MWs was assumed to be 40 km, which is the most sensitive altitude of the weighting functions for the AIRS brightness temperature observations. To determine the initial horizontal wave vectors, the perturbations in the dashed frame in Figure 1 (b) were analyzed using the Lomb–Scargle method (*Scargle* 1982) to derive a 2D Lomb–Scargle periodogram. The wavenumber at the maximum power is $1.2 \times 10^{-2}\mathrm{km}^{-1}$ (λ_H~520 km) and was used as the initial value. The azimuthal angles of the wave vectors at the power maximum are $86°$ and $266°$ clockwise from north. The azimuthal angle has an $180°$ ambiguity due to the 2D spectral analysis. However, the wavenumber vector of a MW is opposite to the background wind over a surface obstacle (*Nappo*, 2002). The zonal wind at 2 km altitude over the Andes mountain chain (Figure 2 (e, f)) is eastward; thus, $266°$ was chosen for the initial azimuthal angle. GW ray tracing was conducted at 9 points ($70° \pm 8°W, 48° \pm 8°S$).

GWs partially break and create local body forces when they reach critical levels or when their non-dimensional amplitudes become large. (*Fritts and Alexander*, 2003). These instabilities are classified into two types: shear instability and convective instability. Our ray tracing analysis can estimate the locations for critical levels of MWs, but cannot identify locations of instabilities. To investigate the occurrence of the instabilities, the Richardson number, R_i, and the ratio between the horizontal wind amplitude (u'_{amp}) and the intrinsic horizontal phase speed (c) were estimated along the ray path of each MW. When $R_i = 0.25$, this indicates the likelihood of shear instability (*Fritts and Alexander*, 2003). Convective

instability occurs when the ratio u'_{amp}/c is larger than 0.7-1 (*Vadas and Becker*, 2019). The temperature amplitude, T'_{amp}, at the initial altitude were derived from the variance of the brightness temperature in the dashed frame in Figure 2 (b). In this case, T'_{amp} is 3 K. u'_{amp} was estimated with the assumption of inertial GW by equation (10) in *Geller and Gong* (2010). The T'_{amp} and u'_{amp} values at the altitude of the next step was calculated from the total GW energy, assuming that the energy increases with an e-folding at twice the density scale height (*Alexander et al.*, 2011; *Kogure et al.*, 2017; *Liu et al.*, 2014; *Lu et al.*, 2015).

Figure 3 (a) shows the ray paths of the MWs superimposed on Figure 2 (b). Figures 3 (b) and (c) shows the vertical profile of the zonal and meridional background wind along each ray path, respectively. Triangles indicate where the waves may have encountered shear instability. Almost all waves encountered critical levels at altitudes of ~60 km, except for two waves that originated at $70°W, 56°S$ and $62°W, 56°S$. These two waves reached the model top (~75 km) of MERRA-2. All waves had a preference to propagate leeward. Moreover, all waves began to meet the shear instability condition at altitudes of ~60 km. Most waves began to meet the convective instability condition a few kilometers higher in altitude than those of the shear instability condition. However, one wave that originated at $62°W, 56°S$ met the convective instability condition at ~10 km higher altitude (~72 km) and two waves originating at $70°W, 56°S$ and $77°W, 56°S$ did not meet the condition (not shown). Since brightness temperature variances observed by AIRS are much smaller than the actual atmospheric temperature variance (*Hoffmann et al.*, 2014), these waves possibly met the conditions at lower altitudes than those in our ray tracing results. These results indicate that the MWs propagated to the region where the concentric ring-like GWs appeared, and then they broke. This result is consistent with the model study of *Vadas and Becker* (2019).

Note that the centers of some concentric ring-like GWs (around $35°E, 60°S$) are far (~1000 km) from the edge of the ray tracing results ($55°E, 56°S$). This horizontal distance can be caused by several possibilities. One possibility is that the secondary GWs were ducted. Although thermal ducts were not found in SABER temperature on July 24 2017 (not shown), we cannot rule out wind ducts. The second possibility is that the background horizontal wind above the observable altitude of AIRS accelerated rapidly in the eastward direction in time. This would cause the MWs to be swept up to thousands of kilometers downstream before breaking (*Vadas and Becker*, 2018). Such acceleration would be difficult to calculate using MERRA-2 winds. Another possibility is that the averaged MERRA-2 winds we used in ray tracing did not represent the winds in the atmosphere. The forth possibility is breaking of primary waves emitted from the polar night jet around $50 - 70°E, 50 - 60°S$ in Figure 1(a) and (b). Those waves may propagate upward, break and generate secondary GWs. Finally, a MW with a large perpendicular component of its wave vector to the zonal wind has a preference to propagate leeward (*Sato et al.*, 2012). Using MERRA-2, we found that the MW was over, and leeward, of the Southern Andes during the event (Figure 3d). The GW perturbations were derived in accordance with *Holt et al.* (2017). The vertical wavelength of these leeward MWs are smaller because they are proportional to the parallel component of a background wind (*Nappo*, 2002). Since AIRS cannot detect GWs with vertical wavelengths less than ~12 km, it is possible for the leeward MWs to be present even though AIRS cannot see them. Indeed, using the AIRS observational filter, we have found that these leeward MWs would have created only small-amplitude perturbations in AIRS which likely would not have been detectable (Figure 3e). However, because these leeward MWs had smaller vertical wavelength, they would have been more susceptible to breaking and

momentum deposition, and therefore would have created the concentric ring-like waves seen by VIIRS.

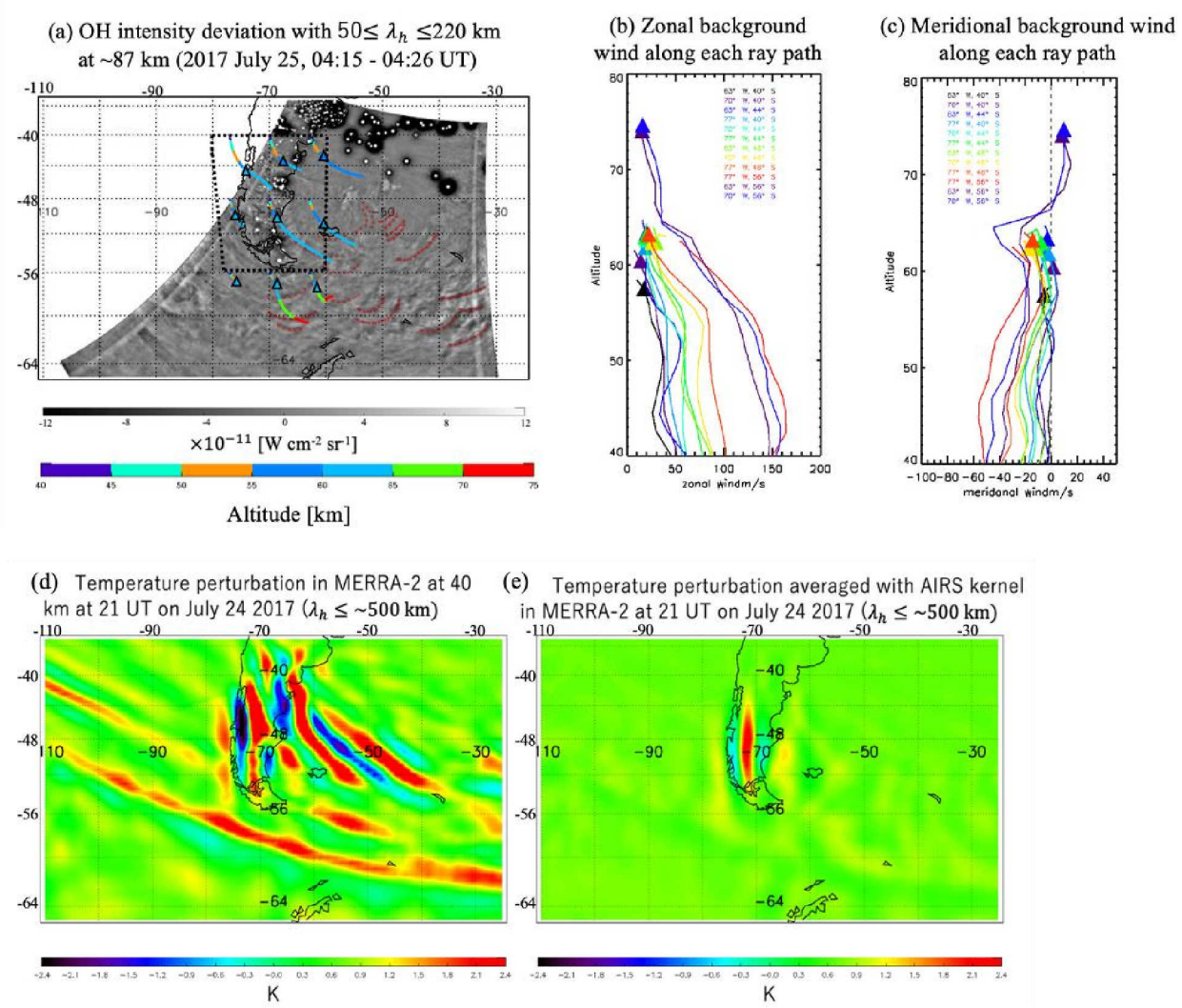

Figure 3. (a) The ray tracing results are superimposed on Figure 2b. The colors indicate the altitude of each MW. The triangles indicate the estimated locations of shear instability. (b) and (c) The vertical profile of the zonal and meridional background wind along each ray path, respectively. (d) Temperature perturbations with horizontal wavelengths less than ~500 km in MERRA-2 at 40 km altitude at 21 UT on July 24 2017. (e) The same as (d), but the temperature perturbation averaged with AIRS kernel.

We also found that the polar night jet is southeastward to the southeast of the Southern Andes. Because the MWs break near or just above the maximum of the polar night jet (where the vertical wavelength decreases rapidly), this means that the secondary GWs would have concentric ring-like structure in the reference frame moving southeastward. Thus, those southward secondary GWs would have larger ground-based horizontal phase speeds than the northward secondary GWs, thereby making the latter more susceptible to critical level absorption and breaking. This is likely why only the southward-propagating branch of the concentric GWs survive to the mesopause region in Fig.3.

We conclude that the concentric ring-like GWs observed here were likely secondary GWs caused by local body forces from breaking MWs. These results are the first direct observational evidence for a similar phenomenon simulated by *Vadas and Becker* (2019) where MWs over the Andes create secondary GWs with a concentric ring-like structure. However, the horizontal wavelengths of the observed secondary GWs (~100 km) were much shorter than those in their model (500-2000 km). This inconsistency could be due to the fact that the minimum horizontal wavelength resolvable by *Vadas and Becker* (2019) was ~165 km (i.e., the model had a horizontal grid spacing of ~65 km). This implies that their model cannot simulate the small-scale concentric GWs observed by VIIRS. Additionally, GWs are only observable in the OH layer if they have vertical wavelengths > 10 km (*Liu and Swenson,* 2003). Since the secondary GW spectrum excited by a local body force is quite broad (Vadas *et al.*, 2003) and many of the large-scale secondary GWs observed in *Vadas and Becker* (2019) have smaller vertical wavelengths, it is possible that they were not seen in the OH airglow layer. In addition, a MW with a larger wavelength than 200 km can cause small-scale instabilities (less than 30 km), i.e., small scale local body forces (*Heale et al.*, 2020a). Finally, although VIIRS can potentially capture GWs with ~1000 km horizontal wavelengths because of its wide field of view, portions of the VIIRS images are frequently contaminated with clouds or city lights, making it difficult to capture large-scale GWs. Thus, VIIRS tends to be sensitive to secondary GWs with smaller horizontal wavelengths than those simulated by *Vadas and Becker* (2019).

5 Conclusion

AIRS captured a MW event with significant brightness temperature amplitudes (3 K) in the stratosphere and ~500 km horizontal wavelengths over the Southern Andes on 24-25 July 2017. During this event, VIIRS did not detect MWs but instead observed concentric ring-like GWs with ~100 km wavelengths at 04:30 UT leeward of the Southern Andes. Our ray tracing result shows that the MWs propagated to the east where the concentric GWs appeared while the MWs were breaking. Thus, the concentric waves were probably secondary GWs generated by local body forces created by the breaking MWs. These observational results are consistent with the model results of *Vadas and Becker* (2019), except for the horizontal wavelengths of the secondary GWs. This difference in horizontal wavelengths could be due to differing coverage of the GW spectrum between the VIIRS observations and the model. This study shows the first concrete evidence that secondary GWs are generated by MWs over the Andes and have concentric or ring-like structures. In addition, this study supports the theory of *Vadas and Becker* (2019) for vertical coupling via secondary and higher-order GWs throughout the middle and upper atmosphere.

Acknowledgments, Samples, and Data

We thank Joan Alexander for her suggestion for the calculation of the temperature perturbations averaged with the AIRS's kernel in MERRA-2. This study was supported by JSPS KAKENHI 19K23465 and the Scientific Committee on Antarctic Research (SCAR) fellowship award 2019. MK was supported by the JSPS grant JRPs-LEAD with DFG program. SLV was supported by NSF grant AGS-1832988 and by NASA grant 80NSSC19K0836. J. Y. was supported by NSF grants AGS-1651394 and AGS-1834222, and by NASA grant 80NSSC19K0836 and 80NSSC20K0628.

VIIRS DNB and M15 data are distributed by the Comprehensive Large Array-data Stewardship System (CLASS) from the National Oceanic and Atmosphere (https://www.avl.class.noaa.gov/saa/products/search?sub_id=0&datatype_family=VIIRS_SDR&submit.x=26&submit.y=9). MERRA-2 data were obtained at http://disc.sci.gsfc.nasa.gov. The AIRS/Aqua gravity wave datasets (Hoffmann et al., 2017) are provided by Forschungszentrum Jülich (https://datapub.fz-juelich.de/slcs/airs/gravity_waves/data). The raytracing model is provided at http://id.nii.ac.jp/1291/00015899/.

References

Alexander, M.J., Geller, M., McLandress, C., Polavarapu, S., Preusse, P., Sassi, F., et al. (2010). Recent developments in gravity-wave effects in climate models and the global distribution of gravity-wave momentum flux from observations and models. *Quarterly Journal of the Royal Meteorological Society*, 136: 1103–1124. doi:10.1002/qj.637

Alexander, S. P., Klekociuk, A. R., & Murphy, D. J. (2011). Rayleigh lidar observations of gravity wave activity in the winter upper stratosphere and lower mesosphere above Davis, Antarctica (69°S, 78°E). *Journal of Geophysical Research*, 116, D13109. doi:10.1029/2010JD015164

Andreassen, Ø, Hvidsten, P., Fritts, D., & Arendt, S. (1998). Vorticity dynamics in a breaking internal gravity wave. Part 1. Initial instability evolution. *Journal of Fluid Mechanics,* 367, 27–46. doi:10.1017/S0022112098001645

Aumann, H. H., Chahine, M. T., Gautier C., Goldberg, M. D., Kalnay E., McMillin, L. M., et al (2003). AIRS/AMSU/HSB on the Aqua mission: Design, science objectives, data products, and processing systems. *IEEE Transactions on Geoscience and Remote Sensing*, *41*(2), 253–264.

Bacmeister, J. T., & Schoeberl, M. R. (1989). Breakdown of Vertically Propagating Two-Dimensional Gravity Waves Forced by Orography. *Journal of the Atmospheric Sciences,* 46, 2109–2134. doi:10.1175/1520-0469(1989)046<2109:BOVPTD>2.0.CO;2

Becker, E., & Vadas S. L. (2018). Secondary gravity waves in the winter mesosphere: Results from a high-resolution global circulation model. *Journal of Geophysical Research: Atmospheres*, 123. doi:10.1002/2017JD027460

Becker, E., & Vadas S. L. (2020). Explicit global simulation of gravity waves in the thermosphere, accepted to *Journal of Geophysical Research: Space Physics*. doi: 10.1029/2020JA028034

Bossert, K., Fritts, D. C., Pautet, P.-D., Williams, B. P., Taylor, M. J., Kaifler, B., et al. (2015). Momentum flux estimates accompanying multiscale gravity waves over Mount Cook, New Zealand, on 13 July 2014 during the DEEPWAVE campaign. *Journal of Geophysical Research: Atmospheres*, 120, 9323–9337. doi:10.1002/2015JD023197

Butchart, N., Cionni, I., Eyring, V., Shepherd, T. G., Waugh, D. W., Akiyoshi, H., et al. (2010). Chemistry–Climate Model Simulations of Twenty-First Century Stratospheric Climate and Circulation Changes. *Journal of Climate*, 23, 5349–5374. doi:10.1175/2010JCLI3404.1

Chahine, M. T., Pagano, T. S., Aumann, H. H., Atlas, R., Barnet, C., Blaisdell, J., et al. (2006). AIRS: Improving Weather Forecasting and Providing New Data on Greenhouse Gases. *Bulletin of the American Meteorological Society,* 87,911–926. doi:10.1175/BAMS-87-7-911

de Wit, R. J., Janches, D., Fritts, D. C., Stockwell, R. G., & Coy, L. (2017). Unexpected climatological behavior of MLT gravity wave momentum flux in the lee of the Southern Andes hot spot. *Geophysical Research Letters*, 44, 1182–1191. doi:10.1002/2016GL072311.

Dunkerton, T.J., (1984). Inertia–Gravity Waves in the Stratosphere. *Journal of the Atmospheric Sciences,* 41, 3396–3404. doi:10.1175/1520-0469(1984)041<3396:IWITS>2.0.CO;2

Ern, M., Hoffmann, L., & Preusse, P. (2017). Directional gravity wave momentum fluxes in the stratosphere derived from high-resolution AIRS temperature data. *Geophysical Research Letters*, 44, 475–485. doi:10.1002/2016GL072007

Fritts, D. C., Isler, J. R., & Andreassen, Ø. (1994). Gravity wave breaking in two and three dimensions: 2. Three-dimensional evolution and instability structure. *Journal of Geophysical Research*, 99(D4), 8109– 8123. doi:10.1029/93JD03436

Fritts, D. C., Arendt S., & Anderassen, Ø. (1998). Vorticity dynamics in a breaking internal gravity wave. Part 2. Vortex interactions and transition to turbulence. *Journal of Fluid Mechanics*, 367, 47-65. doi:10.1017/S0022112098001633

Fritts, D. C., & Alexander, M. J. (2003). Gravity wave dynamics and effects in the middle atmosphere. *Reviews of Geophysics*, 41, 1003. doi:10.1029/2001RG000106, 1

Gelaro, R., McCarty, W., Suárez, M. J., Todling, R., Molod, A., Takacs, L., et al. (2017). The Modern-Era Retrospective Analysis for Research and Applications, Version 2 (MERRA-2). *Journal of Climate,* 30, 5419–5454. doi.org/10.1175/JCLI-D-16-0758.1

Geller, M. A., & Gong, J. (2010). Gravity wave kinetic, potential, and vertical fluctuation energies as indicators of different frequency gravity waves. *Journal of Geophysical Research*, 115, D11111. doi:10.1029/2009JD012266

Heale, C. J., Bossert, K., Snively, J. B., Fritts, D. C., Pautet, P.-D., & Taylor, M. J. (2017), Numerical modeling of a multiscale gravity wave event and its airglow signatures over Mount Cook, New Zealand, during the DEEPWAVE campaign. *Journal of Geophysical Research: Atmospheres,* 122, 846–860. doi:10.1002/2016JD025700

Heale, C. J., Bossert, K., Vadas, S. L., Hoffmann, L., Dörnbrack, A., Stober, G., J. B. Snively, & C. Jacobi (2020a). Secondary gravity waves generated by breaking mountain waves over

Europe. *Journal of Geophysical Research: Atmospheres*, 125, e2019JD031662. doi:10.1029/2019JD031662

Heale, C. J., Lund, T., & Fritts, D. C. (2020b). Convectively generated gravity waves during solstice and equinox conditions. *Journal of Geophysical Research: Atmospheres*, 125, e2019JD031582. doi:10.1029/2019JD031582

Hoffmann, L., Xue, X., & Alexander, M. J. (2013). A global view of stratospheric gravity wave hotspots located with Atmospheric Infrared Sounder observations. *Journal of Geophysical Research: Atmospheres*, 118, 416– 434. doi:10.1029/2012JD018658

Hoffmann, L., Alexander, M. J., Clerbaux, C., Grimsdell, A. W., Meyer, C. I., Rößler, T., & Tournier, B., (2014). Intercomparison of stratospheric gravity wave observations with AIRS and IASI. *Atmospheric Measurement Techniques*, 7, 4517–4537. doi.org/10.5194/amt-7-4517-2014

Hoffmann, L., Spang, R., Orr, A., Alexander, M. J., Holt, L. A., & Stein, O., (2017). A decadal satellite record of gravity wave activity in the lower stratosphere to study polar stratospheric cloud formation. *Atmospheric Chemistry and Physics*, 17, 2901–2920. doi:10.5194/acp-17-2901-2017

Kogure, M., Nakamura, T., Ejiri, M. K., Nishiyama, T., Tomikawa, Y., & Tsutsumi, M. (2018). Effects of horizontal wind structure on a gravity wave event in the middle atmosphere over Syowa (69°S, 40°E), the Antarctic. *Geophysical Research Letters*, 45, 5151–5157. doi:10.1029/2018GL078264

Kogure, M., Nakamura, T., Ejiri, M. K., Nishiyama, T., Tomikawa, Y., Tsutsumi, M., et al. (2017). Rayleigh/Raman lidar observations of gravity wave activity from 15 to 70 km altitude over Syowa (69°S, 40°E), the Antarctic. *Journal of Geophysical Research: Atmospheres*, 122, 7869–7880. doi:10.1002/2016JD026360

Liu, A. Z., & Swenson, G. R. (2003). A modeling study of O_2 and OH airglow perturbations induced by atmospheric gravity waves. *Journal of Geophysical Research*, 108, 4151. doi:10.1029/2002JD002474, D4

Liu, X., Yue, J., Xu, J., Wang, L., Yuan, W., Russell, J. M., & Hervig, M. E. (2014). Gravity wave variations in the polar stratosphere and mesosphere from SOFIE/AIM temperature observations. *Journal of Geophysical Research: Atmospheres*, 119, 7368–7381. doi:10.1002/2013JD021439

Lu, X., Chu, X., Fong, W., Chen, C., Yu, Z., Roberts, B. R., & McDonald, A. J. (2015). Vertical evolution of potential energy density and vertical wave number spectrum of Antarctic gravity waves from 35 to 105 km at McMurdo (77.8°S, 166.7°E). *Journal of Geophysical Research: Atmospheres*, 120, 2719–2737. doi:10.1002/2014JD022751

Liu, X., Xu, J., Yue, J., Vadas, S. L., & Becker, E. (2019). Orographic primary and secondary gravity waves in the middle atmosphere from 16-year SABER observations. *Geophysical Research Letters*, 46, 4512–4522. doi:10.1029/2019GL082256

Marks, C. J., & Eckermann, S.D. (1995). A Three-Dimensional Nonhydrostatic Ray-Tracing Model for Gravity Waves: Formulation and Preliminary Results for the Middle Atmosphere. *Journal of the Atmospheric Sciences,* **52**, 1959–1984. doi:10.1175/1520-0469(1995)052<1959:ATDNRT>2.0.CO;2

Miller D. S., William C. S., Jia Y., Steven M. S., Alexander, M. J., Lars H., et al. (2015). Upper atmospheric gravity wave details revealed in nightglow satellite imagery. *Proceedings of the National Academy of Sciences* 112 (49) E6728-E6735. doi: 10.1073/pnas.1508084112

Nappo, C. J. (2002), *An Introduction to Atmospheric Gravity Waves*. *Academic Press*, 260.

O'sullivan, D., & T. J. Dunkerton (1995). Generation of Inertia–Gravity Waves in a Simulated Life Cycle of Baroclinic Instability. *Journal of the Atmospheric Sciences*, 52, 3695–3716, doi:10.1175/1520-0469(1995)052<3695:GOIWIA>2.0.CO;2.

Preusse, P., Eckermann, S. D., Ern, M., Oberheide, J., Picard, R. H., Roble, R. G., et al. (2009). Global ray tracing simulations of the SABER gravity wave climatology. *Journal of Geophysical Research*, 114, D08126. doi:10.1029/2008JD011214

Sato, K., Tateno, S., Watanabe, S., & Kawatani, Y. (2012). Gravity Wave Characteristics in the Southern Hemisphere Revealed by a High-Resolution Middle-Atmosphere General Circulation Model. *Journal of the Atmospheric Sciences,* 69, 1378–1396. doi:10.1175/JAS-D-11-0101.1

Sato, K., & Yoshiki, M. (2008). Gravity Wave Generation around the Polar Vortex in the Stratosphere Revealed by 3-Hourly Radiosonde Observations at Syowa Station. *Journal of the Atmospheric Sciences,* 65, 3719–3735. doi:10.1175/2008JAS2539.1

Smith, S., Baumgardner, J., & Mendillo, M. (2009). Evidence of mesospheric gravity-waves generated by orographic forcing in the troposphere. *Geophysical Research Letters*, 36, L08807. doi:10.1029/2008GL036936

Taylor, M. J., & Hapgood, M. A. (1988), Identification of a thunderstorm as a source of short period gravity waves in the upper atmospheric nightglow emissions, *Planetary and space science*, 36(10), 975–985. doi:10.1016/0032-0633(88)90035-9

Tomikawa, Y. (2015). Gravity wave transmission diagram. Ann. Geophys., 33, 1479–1484. doi.org/10.5194/angeo-33-1479-2015

Trinh, Q. T., M. Ern, E. Doornbos, P. Preusse, & M. Riese (2018). Satellite observations of middle atmosphere-thermosphere vertical coupling by gravity waves. Annals of *Geophysics*, 36, 425–444. doi:10.5194/angeo-36-425-2018

Vadas, S. L., Fritts, D. C., & Alexander M. J. (2003). Mechanism for the Generation of Secondary Waves in Wave Breaking Regions. *Journal of the Atmospheric Sciences,* 60, 194–214. doi:10.1175/1520-0469(2003)060<0194:MFTGOS>2.0.CO;2

Vadas, S. L, Jia Y., Joe S., Pete S., & Alan L., (2009). A model study of the effects of winds on concentric rings of gravity waves from a convective plume near Fort Collins on 11 May 2004. *Journal of Geophysical Research,* 114, D06103. doi:10.1029/2008JD010753

Vadas, S.L and G. Crowley, (2010), Sources of the traveling ionospheric disturbances observed by the ionospheric TIDDBIT sounder near Wallops Island on October 30, 2007, J. Geophys. Res. Space Physics, 115, A07324, doi:10.1029/2009JA015053.

Vadas, S. L., Yue J., & Nakamura T., (2012). Mesospheric concentric gravity waves generated by multiple convection storms over the North America Great Plain. *Journal of Geophysical Research*, 117, D7. doi:10.1029/2011JD017025

Vadas, S. L., & Becker, E.(2018). Numerical modeling of the excitation, propagation, and dissipation of primary and secondary gravity waves during wintertime at McMurdo Station in the Antarctic. *Journal of Geophysical Research: Atmospheres*, 123, 9326–9369. doi:10.1029/2017JD027974

Vadas, S. L., Zhao, J., Chu, X., & Becker E., (2018). The excitation of secondary gravity waves from local body forces: Theory and observation. *Journal of Geophysical Research: Atmospheres*, 123, 9296–9325. doi:10.1029/2017JD027970

Vadas, S. L., & Becker, E. (2019). Numerical modeling of the generation of tertiary gravity waves in the mesosphere and thermosphere during strong mountain wave events over the Southern Andes. *Journal of Geophysical Research: Space Physics*, 124, 7687–7718. doi:10.1029/2019JA026694

Vadas, S. L., Xu, S., Yue, J., Bossert, K., Becker, E., & Baumgarten, G., (2019). Characteristics of the Quiet-time Hotspot Gravity Waves Observed by GOCE over the Southern Andes on 5 July 2010. *Journal of Geophysical Research: Space Physics*, 124, 7034–7061. doi.org/10.1029/2019JA026693

Vargas, F., Swenson, G., Liu, A., & Pautet, D. (2016). Evidence of the excitation of a ring-like gravity wave in the mesosphere over the Andes Lidar Observatory. *Journal of Geophysical Research: Atmospheres*, 121, 8896–8912. doi:10.1002/2016JD024799

Wu, D. L., & Eckermann, S. D. (2008). Global Gravity Wave Variances from Aura MLS: Characteristics and Interpretation. *Journal of the Atmospheric Sciences*, 65, 3695–3718. doi:org/10.1175/2008JAS2489.1

574

575 **Figure 1**.

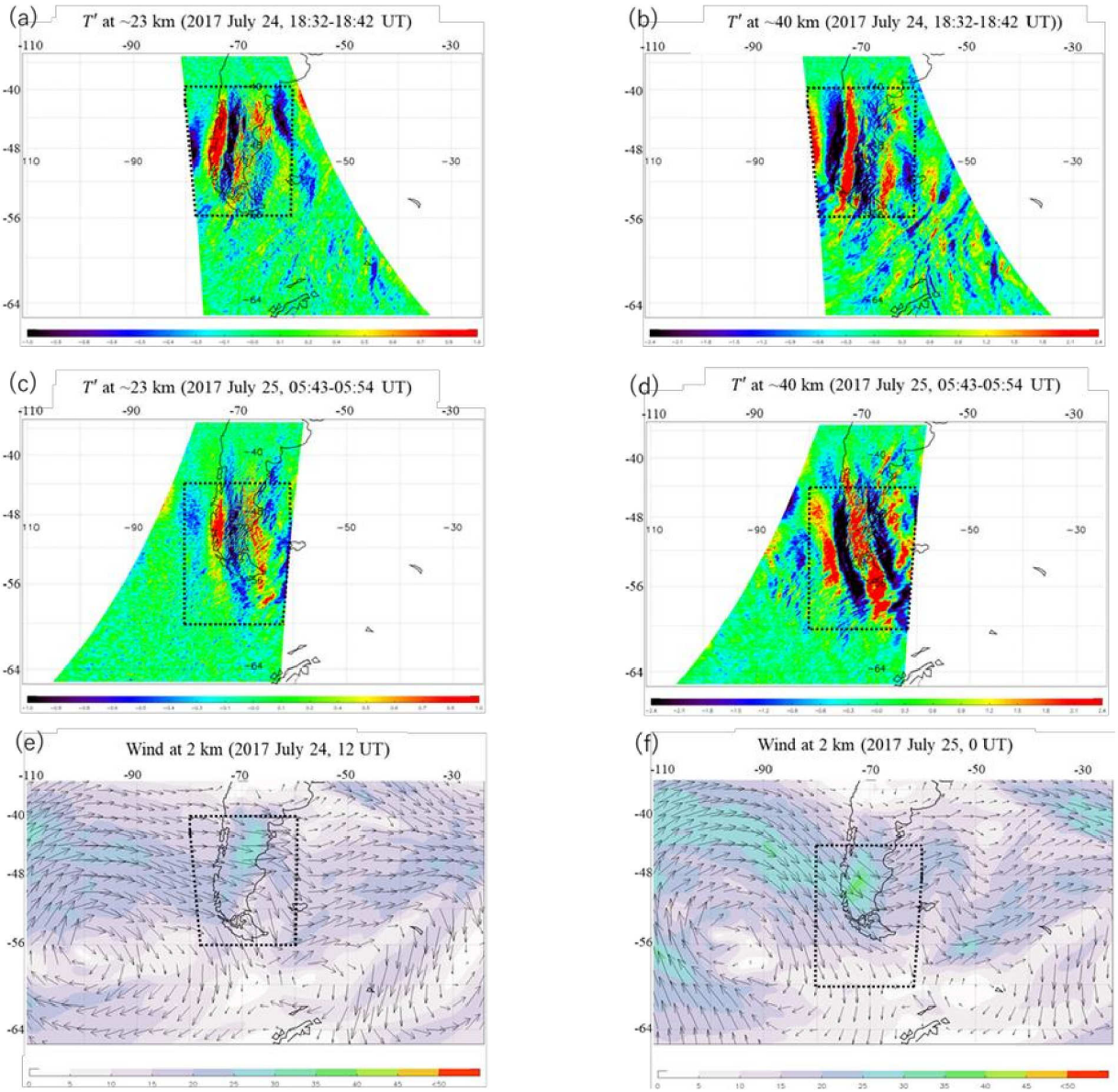

576
577 Figures 1. (a) and (b) show brightness temperature perturbations with GWs at altitudes of ~23
578 and ~40 km in 18:32-18:42 on 24 July 2017, respectively. (c) and (d) show the same as a and b,
579 respectively, but in 05:43-05:54 on 25 July 2017. (e) and (f) show wind at an altitude of 2 km at
580 12 UT on 24 July and 0 UT on 25 July, respectively.
581

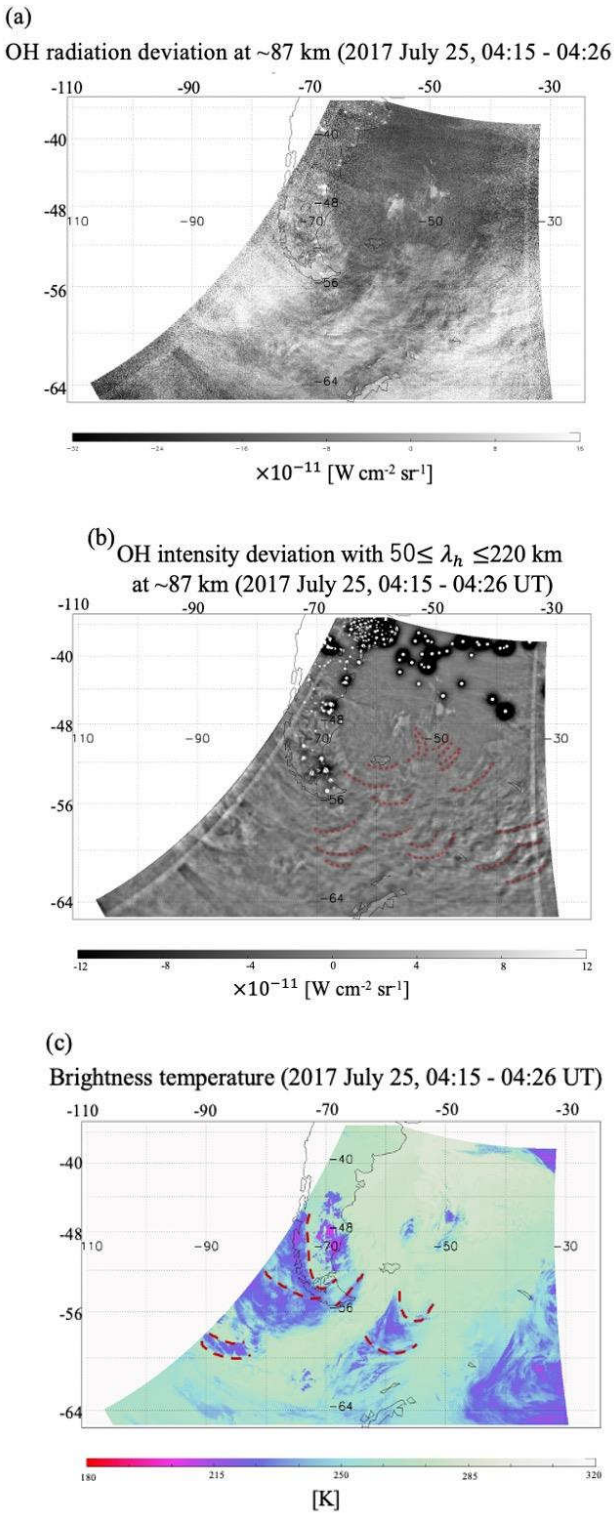

582

583 **Figure 2**. (a) An OH intensity deviation at an altitude of ~87 km in 04:15-04:26 on 25 July 2017.
584 (b) The same as (a), but the deviation is applied with a bandpass Butterworth filter, with a
585 bandpass between 50 and 220 km. (c) shows brightness temperatures of clouds at 9.8-11.8 μm.

Figure 3.

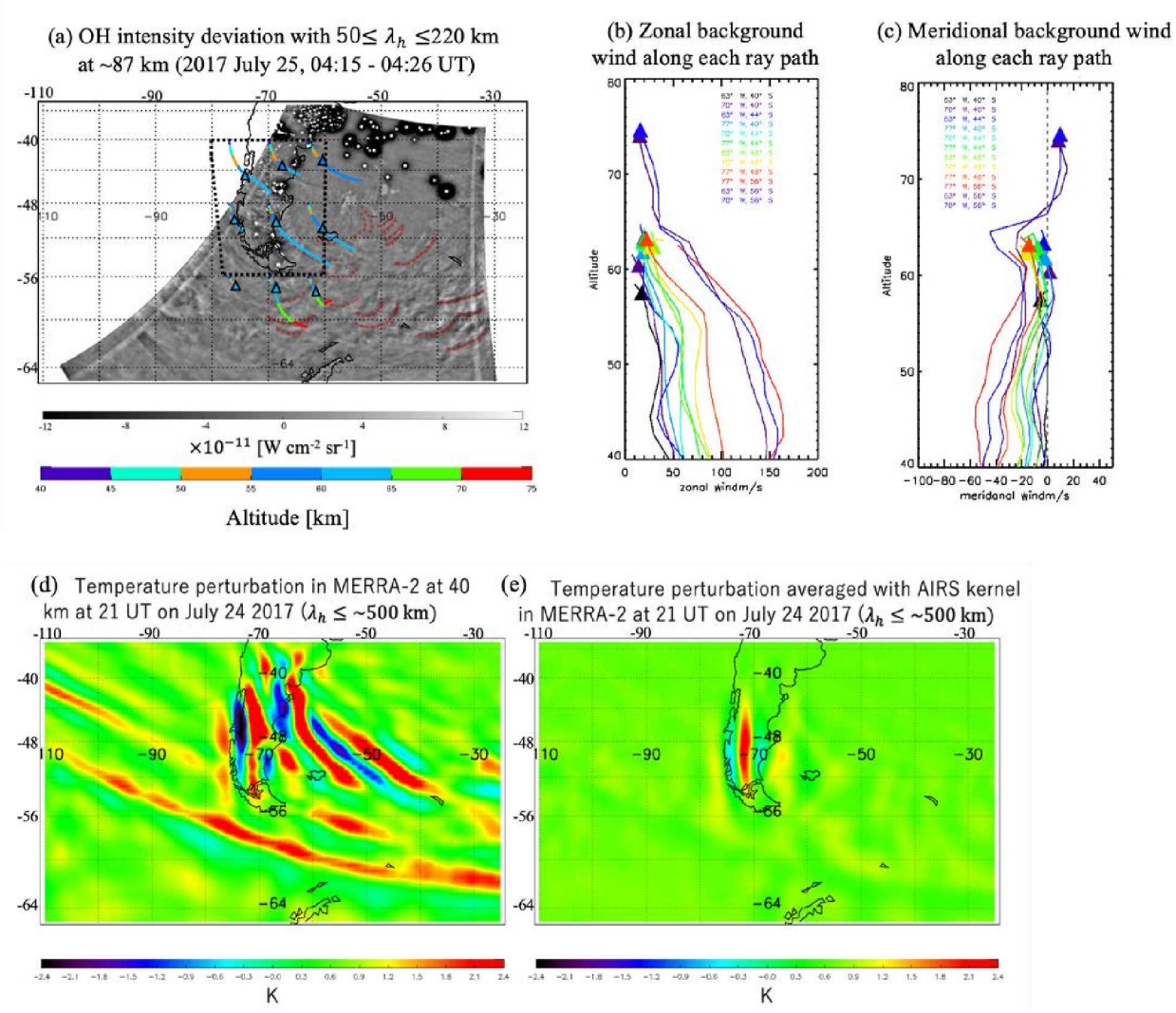

Figure 3. (a) The ray tracing results are superimposed on Figure 2b. The colors indicate the altitude of each MW. The triangles indicate the estimated locations of shear instability. (b) and (c) The vertical profile of the zonal and meridional background wind along each ray path, respectively. (d) Temperature perturbations with horizontal wavelengths less than ~500 km in MERRA-2 at an altitude of 40 km at 21 UT on July 24 2017. (e) The same as (d), but the temperature perturbation averaged with AIRS kernel.